

## Article

# Study on the Hydraulic Characteristics of an Eccentric Tapering Outlet Pressure Box Culvert in a Pumping Station

Ye-Xin Chen, Bin Xi \*, Zhigang Chen and Shixuan Shen

College of Hydraulic Science and Engineering, Yangzhou University, Yangzhou 225009, China; cheneyxin\_2022@163.com (Y.-X.C.)

\* Correspondence: bxi@yzu.edu.cn

**Abstract:** The outlet pressure box culvert is often used as the drainage building of a pumping station. Because of its compact structure, it produces transverse flow velocity and then forms poor flow patterns, such as bias flow, reflux, and flow separation, which affect the discharge efficiency of the pumping station. Based on the combination of a physical model test and numerical simulation, the hydraulic characteristics of an eccentric tapering outlet pressure box culvert were analyzed. Focusing on the poor flow pattern in the box culvert, different optimization schemes were proposed to adjust the flow pattern. The flow pattern, transverse velocity distribution ratio (which represents the proportion of transverse velocity in velocity), average angle of the axial velocity, axial velocity uniformity, and pressure distribution of each scheme were compared to obtain the best scheme. The results show that the combination scheme of “diversion pier position and angle with deflecting flow baseplate” has the best optimization effect on the flow pattern. This scheme can effectively improve the bad flow pattern, significantly reduce the transverse velocity distribution ratio, and make the pressure distribution on both sides of the long diversion pier uniform. The axial velocity uniformity was increased by 17.45%, and the average angle of the axial velocity was increased by 8.23°.

**Keywords:** eccentric tapering outlet pressure box culvert; model test; numerical simulation; optimization scheme; average angle of the axial velocity



**Citation:** Chen, Y.-X.; Xi, B.; Chen, Z.; Shen, S. Study on the Hydraulic Characteristics of an Eccentric Tapering Outlet Pressure Box Culvert in a Pumping Station. *Processes* **2023**, *11*, 1598. <https://doi.org/10.3390/pr11061598>

Academic Editors: Wenjie Wang, Giorgio Pavesi, Jin-Hyuk Kim, Ji Pei and Lijian Shi

Received: 11 April 2023

Revised: 18 May 2023

Accepted: 22 May 2023

Published: 23 May 2023



**Copyright:** © 2023 by the authors. Licensee MDPI, Basel, Switzerland. This article is an open access article distributed under the terms and conditions of the Creative Commons Attribution (CC BY) license (<https://creativecommons.org/licenses/by/4.0/>).

## 1. Introduction

The pressure box culvert is often used as the drainage building of a drainage pumping station. Compared with the open outlet pool, the pressure outlet box culvert has the advantages of small size and reduced engineering requirements. However, with the rise in global temperature, frequent flood disasters have put pressure on the operation of many current pumping stations. In an actual project, the current pumping stations cannot meet the requirements of the pumping flow; therefore, they need to be expanded and renovated. However, the expansion of a pumping station is restricted by the project site; consequently, the eccentric tapering outlet pressure box culvert with a smaller footprint is used as the drainage building. The internal structure of the eccentric tapering outlet pressure box culvert is compact, and the number of pressure ducts is less than the number of pumping station units. The phenomenon of inconsistent confluence occurs in the culvert, resulting in a poor flow pattern in the box culvert and affecting the efficiency of the pumping station outflow. Therefore, it is of great importance to improve the outflow efficiency of the pumping station by analyzing the hydraulic characteristics of the eccentric tapering outlet pressure box culvert and by adopting the appropriate optimization schemes to eliminate the bad flow pattern.

In the past, the study of the hydraulic characteristics of the inlet and outlet structures of the pumping station mainly relied on physical model tests. The flow velocity data of the feature points were collected by a flow meter, or the flow field data were collected by digital particle image velocimetry (DPIV). In recent years, computational fluid dynamics (CFD)

technology has gradually matured and has become an important means of studying the flow pattern in hydraulic engineering [1–9]. Recently, using CFD technology, scholars have studied the hydraulic characteristics and rectification measures of the inlet and outlet structures of the pumping station. Luo et al. [10,11] proposed a rectification scheme based on computational fluid dynamics to optimize the flow pattern of the forebay. Kadam et al. [12] used a combination of physical model and numerical simulation to study the flow field of the inlet building of a pumping station. It was found that the large diffusion angle of the forebay and the small submergence depth were the causes of the poor flow pattern. Zhao et al. [13] adopted the combined rectification scheme of a diversion wall and vertical column; with the scheme, they were able to eliminate the recirculation zone in the forebay and to improve the axial velocity uniformity. Using the realizable  $k-\epsilon$  model, Zhang et al. [14] studied the flow pattern of a lateral pumping station. Chen et al. [15] used the finite volume method to solve the control equation and carried out a numerical simulation and experiment on a multi-inlet pumping station. They found that the numerical simulation results were consistent with the physical experiment results. Xia et al. [16] found that a single row of a vertical column arranged in the front middle of the forebay could effectively improve the flow pattern of the forebay. In the field of fluid machinery optimization, CFD technology is also used as a common means [17,18].

Previous studies have focused on the study of the flow pattern and rectification measures of the forebay and inlet pool of the pumping station. However, there are few studies on the eccentric tapering outlet pressure box culvert. Therefore, in this paper, the numerical model and the physical model test are combined to optimize the flow pattern of the eccentric tapering outlet pressure box culvert in the original scheme. The combined optimization scheme for the internal structure of the box culvert is discussed, and the hydraulic characteristics of each scheme are studied [19–23]. The analysis process is shown in Figure 1.

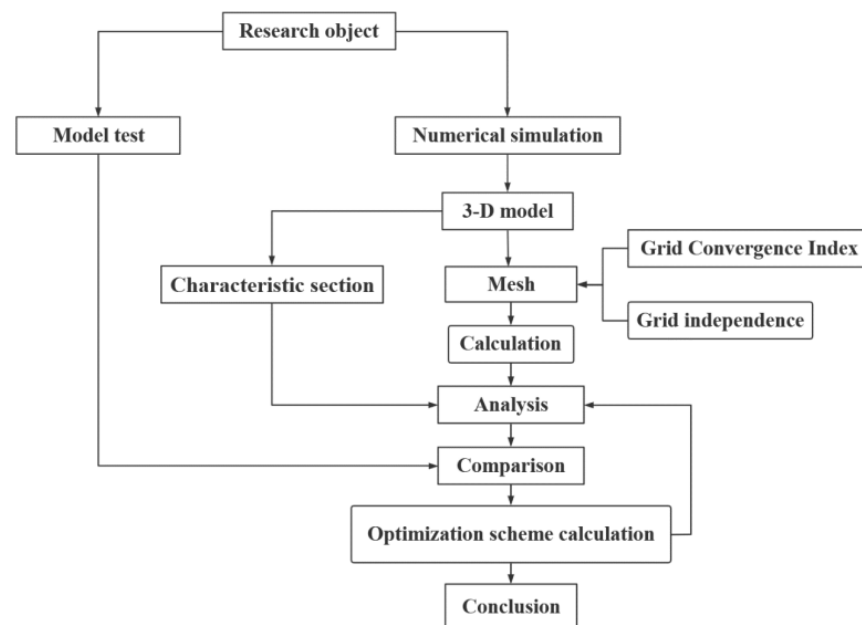


**Figure 1.** Flowchart for the study process.

The innovation of the research lies in the combination of numerical calculation and a model test, and some new evaluation indexes are proposed to evaluate the optimization effect of each scheme. For example, in view of the transverse bias flow in the box culvert, an evaluation index of the transverse velocity distribution ratio is proposed to quantitatively describe the transverse bias flow. According to the distribution of pressure on both sides of the long diversion pier, the rationality of the structural arrangement in the box culvert is evaluated. Finally, the best scheme is selected by combining the above indexes with the

axial velocity uniformity, the average angle of the axial velocity, and the flow pattern of the characteristic section. The research results of this paper can provide a reference for the design of a similar pressure box culvert.

## 2. Physical Model Test and Numerical Simulation

### 2.1. Project Overview

In this paper, a pumping station project was taken as the research background. Due to the insufficient pumping and discharging capacity of the current pumping station, the right side of the current pumping station was expanded and reconstructed to meet the pumping and discharging needs. The expanded pumping station has four units numbered 1#~4#. The design flow of each unit is  $12.25 \text{ m}^3/\text{s}$ , and the total design flow of the expanded pumping station is  $49.00 \text{ m}^3/\text{s}$ . A pressure box culvert is used as a drainage building in the current pumping station. Due to the limitations of the project land, an eccentric tapering outlet pressure box culvert is used as a drainage building at the side of the expanded pumping station. The length of the eccentric tapering outlet pressure box culvert along the flow direction is 28.20 m, and the length of the pressure culvert along the flow direction is 18.80 m. The elevation of the top of the box culvert was obliquely reduced from 14.60 m to 11.00 m. The elevation of the deflecting flow baseplate is 9.50 m, and the elevation of the box culvert floor is 6.00 m. Figure 2 shows the schematic diagram of the project plane and the layout of the eccentric tapering outlet pressure box culvert section.

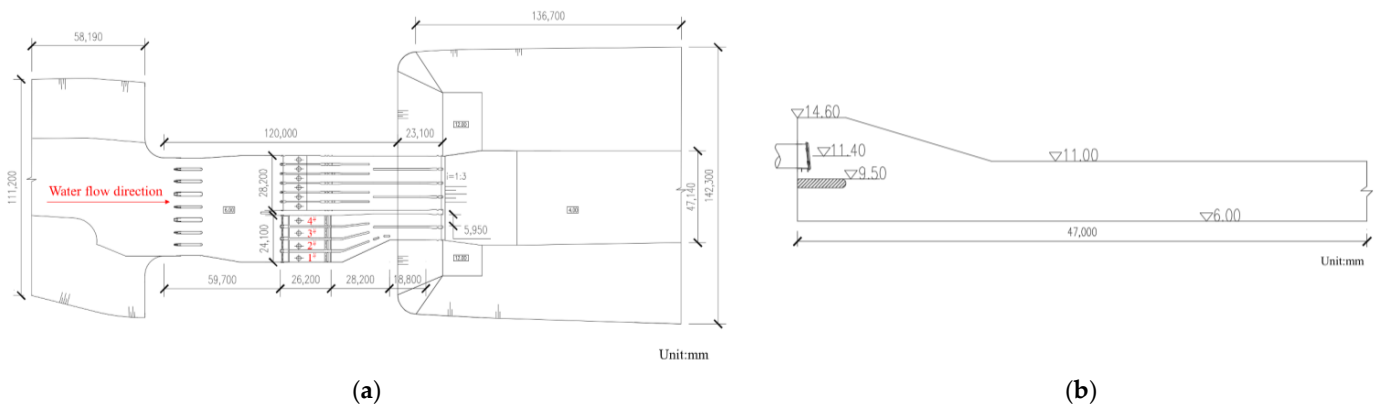


**Figure 2.** Engineering schematic diagram: (a) engineering plane diagram; (b) section diagram of box culvert.

### 2.2. Physical Model

#### 2.2.1. Similarity Criterion

In order to ensure that the test model results and prototype results fit each other, certain similarity conditions and similarity criteria must be observed in the model tests. In the case of turbulence, the velocity of the water flow and the fluctuation of the water surface are strongly affected by gravity. In this case, the force that played a decisive role was gravity, and it was possible to satisfy the test requirements with a design made according to the gravity similarity criterion. According to the size and layout of the pumping station, the geometric scale of the model was determined as  $L_r = 40$  [24,25]. According to the similarity criterion, we obtain the following:

Velocity scale

$$\text{Velocity scale : } V_r = L_r^{0.5} = 6.32;$$

$$\text{Quantity scale : } Q_r = L_r^{2.5} = 10,119.29;$$

$$\text{Roughness scale : } n_r = L_r^{1/6} = 1.85.$$

In order to ensure that the roughness of each part of the model is similar to that of the prototype, different model materials should be used to make the model. The prototype outlet pressure box culvert was made of reinforced concrete, and its roughness was 0.016; therefore, the corresponding model roughness was 0.0086. The model outlet pressure box culvert was made of transparent organic glass plate, which met the roughness requirements and facilitated the observation of the water flow pattern in the pressure box culvert.

### 2.2.2. Model Layout

The physical model included the forebay, outlet pressure box culvert, eccentric tapering outlet pressure box culvert, electromagnetic flowmeter, circulating pump, outlet sump, and so on. Figure 3 shows the layout of the test model.

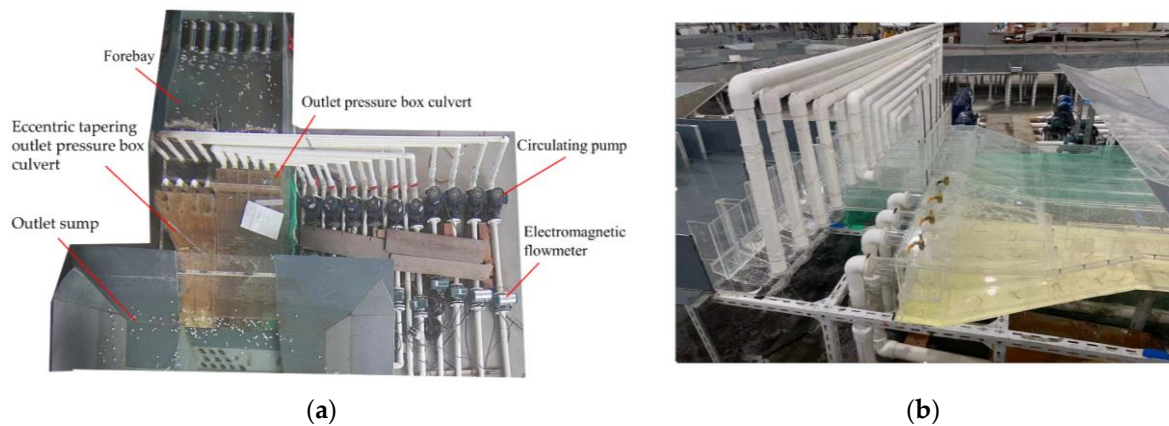


**Figure 3.** Test model layout: (a) general layout of the model; (b) local layout of outlet pressure box culvert.

The physical model adopted the internal circulation water flow system. In order to control and measure the flow rate of each unit, the inlet and outlet conduits were separated, and the valves, electromagnetic flow meters, and circulating power pumps were connected in turn with pipes of the same diameter as the inlet and outlet water conduits, forming an independent control and flow measurement system for each unit to meet the needs of the test. In the physical model experiment, an LGY-III multi-functional intelligent flowmeter was used to measure the flow velocity of the feature points. It was able to synchronously measure eight flow velocities to achieve a multi-point synchronous measurement of flow and to reduce the effect of measurement errors. The velocity can be calculated by Equation (1).

$$V = \lambda_v \times (K \times N/T + C) \quad (1)$$

where  $V$  is the velocity, cm/s;  $\lambda_v$  is the velocity scale;  $K$  and  $C$  are the calibration coefficients of the flow rate sensor;  $N$  is the number of sensors spinning pulses during the sampling time; and  $T$  is the sampling time, s.

### 2.2.3. Flow Pattern Study

It is necessary for the outflow from unit 1 and unit 2 to enter the No.1 pressure duct and for the outflow from unit 3 and unit 4 to enter the No.2 pressure duct. If the unit outflow cannot enter the corresponding pressure duct, it will lead to different shunt volumes on both sides of the long diversion pier, resulting in a pressure difference on both sides. In order to study the flow distribution of the unit outflow at the inlet end of the long diversion pier, the tracer liquid was uniformly applied in the box culvert to characterize it. In Figure 4a, it can be clearly seen that the outflow of unit 3 is diverting at the inlet end of the long diversion pier. This is because the arrangement of the long diversion pier is unreasonable. The outflow of unit 3 cannot enter the No.2 pressure duct in a completely

straight manner. It diverges at the inlet end of the long diversion pier, and part of the water flows into the No.1 pressure duct. Red silk lines were arranged at the bottom of the box culvert. The red silk lines swing with the flow of water, and the direction of the swing represents the flow direction of the water at the bottom of the box culvert. As shown in Figure 4b, the water backflow occurs at the bottom of the pressure box culvert and under the deflecting flow baseplate, and the experimental observation shows that the oscillating velocity of the silk line at the bottom of the deflecting flow baseplate is obviously slower than that at the bottom of the box culvert.

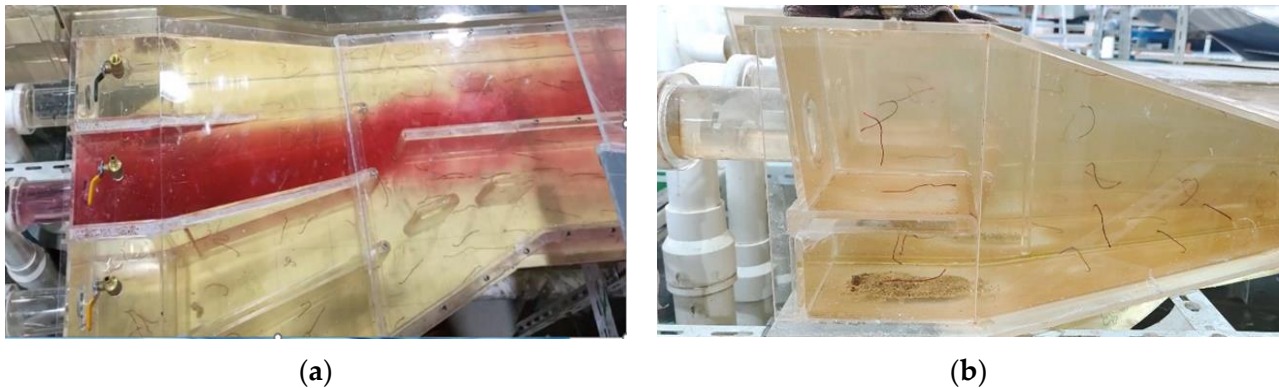


**Figure 4.** Model test of box culvert flow pattern: (a) flow pattern at inlet end of long diversion pier; (b) flow pattern at the bottom of box culvert.

### 2.3. Numerical Simulation

With the physical model, it was difficult to collect the data of the specific section, and the experiment was also limited by the model size and scale effect. Therefore, the research needed to be supplemented by numerical simulation. Numerical simulation has the advantages of low cost and convenient data collection, making it convenient for the comparison and selection of multi-optimization schemes, but its simulation results need to be verified by physical model tests. The combination of the two allows a more comprehensive and accurate study of the hydraulic characteristics of the eccentric tapering outlet pressure box culvert.

#### 2.3.1. Geometric Model

Firstly, it was necessary to model the research object. UG 12.0 software was used to establish a three-dimensional entity model of the eccentric tapering outlet pressure box culvert, whose structure is shown in Figure 5.

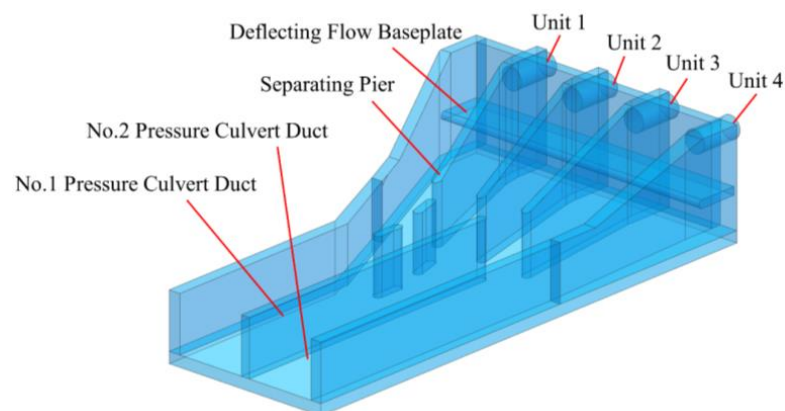


**Figure 5.** Three-dimensional model of the numerical simulation area.

After the model was established, the accuracy of the boundary conditions was an important factor affecting the numerical simulation results. The setting of boundary conditions is referred to in the literature [26]. The velocity inlet condition was adopted as the inlet boundary at the outlets of the outlet conduits of the four units from No.1 to No.4; the outlet boundary was set at the pressure duct outlet for the outflow, and the outlet pressure box culvert side walls and bottom were set as fixed boundaries with no-slip wall surfaces. The solver is the pressure-based solver, which belongs to the commercial software Fluent. The velocity formulation selects the absolute velocity, and the time type is steady state. The SIMPLEC algorithm and the second-order upwind scheme were used to simulate the flow pattern in the box culvert [27].

### 2.3.2. Governing Equations and Turbulent Flow Models

The laws of fluid motion comply with the laws of physical conservation. The conservation laws consist mainly of the law of conservation of energy, the law of conservation of momentum, and the law of conservation of mass. Considering that the heat exchange of the fluid over a short time period has a minimal effect on the model flow regime, the heat exchange of the model was not considered. The continuity equation is described as Equation (2).

$$\frac{\partial u_i}{\partial x_i} = 0 \quad (2)$$

The momentum equation is also called the N-S equation; it can be presented as Equation (3).

$$\frac{\partial(\rho u_i)}{\partial t} + \frac{\partial(\rho u_i u_j)}{\partial x_j} = -\frac{\partial p}{\partial x_i} + \frac{\partial}{\partial x_j} \left[ \mu_{eff} \left( \frac{\partial u_i}{\partial x_j} + \frac{\partial u_j}{\partial x_i} \right) \right] + \rho g_i \quad (3)$$

where  $u_i$  and  $u_j$  are the velocity vector in all directions;  $x_i$  and  $x_j$  represent each coordinate axis;  $\rho$  is the density of the fluid;  $t$  is time;  $p$  is the static pressure of turbulent kinetic energy;  $\mu_{eff}$  is the effective viscosity coefficient of the fluid;  $\rho g_i$  is the gravity component in the  $i$  direction.

The  $k-\varepsilon$  model and the  $k-\omega$  model are the most widely used two-equation models. When simulating the flow pattern in the box culvert, the  $k-\varepsilon$  model was usually used. The turbulent  $k-\varepsilon$  model assumes that eddy viscosity is related to turbulent kinetic energy and dissipation rate, and it introduces turbulent kinetic energy  $k$  and dissipation rate  $\varepsilon$  to solve the turbulent viscosity coefficient. The realizable  $k-\varepsilon$  model constrains the Reynolds stress to ensure the consistency between the Reynolds stress and the real turbulence, and it has higher accuracy for the simulation of large flow changes and flow separation problems. In the physical model experiment, it was observed that the water flow in the pressure box culvert changed greatly and that there was a backflow phenomenon. The realizable  $k-\varepsilon$  model has a good calculation performance in this kind of calculation [28]. Therefore, the realizable  $k-\varepsilon$  model was used in this paper.

### 2.3.3. Grid Independence Analysis

The grid is the basis of the spatial discretization of the governing equations. There are two common types of grid: the structured grid and the unstructured grid. The unstructured grid has no regular topology structure and has the advantage of strong self-adaptation. For the pressure outlet box culvert model with a complex structure, the calculation grid uses the unstructured grids. In the process of dividing the grid, the numerical solution gradually approaches the true solution as the number of grids is continuously increased. However, with the increasing number of grids, the numerical solutions do not vary much from the numerical simulations and are close to the true solutions. At this point, the time consumed by the further refinement of the grid increases greatly, but the computational accuracy does not change much; therefore, the number of grids can be considered irrelevant to the solution results after the error between the numerical solution and the true solution

is less than a certain error. The hydraulic loss of the calculation model is used to verify the independence of the grid, and the changes in the hydraulic loss under different numbers of grids are compared [29]. The hydraulic loss is calculated by Equation (4).

$$h_f = \frac{p_{in} - p_{out}}{\rho g} \quad (4)$$

where  $p_{in}$  is the total pressure at the inlet of the inlet conduit, Pa;  $p_{out}$  is the total pressure at the inlet of the pressure outlet, Pa;  $\rho$  is the water density,  $1 \times 10^3 \text{ kg/m}^3$ ; and  $g$  is gravitational acceleration,  $9.8 \text{ m}^2/\text{s}$ . As shown in Figure 6, it was found that the head loss in the calculation area did not change much when the number of grids exceeded  $162 \text{ w}$ . The number of mesh in this calculation is determined to be 1,628,496, and the grid nodes are 301,410. It can be considered that the grid calculation results were independent of the density of the grid division; other models with the same density are calculated in this paper.

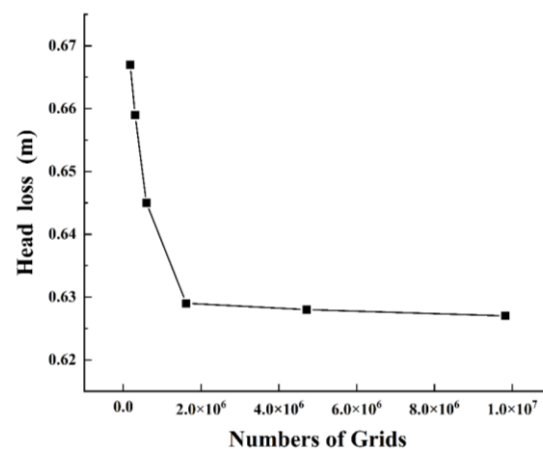


Figure 6. Hydraulic loss diagram under different grid conditions.

#### 2.3.4. Convergence of Grid

In order to reduce the influence of the computational grid on the numerical simulation results, the grid convergence index (GCI) method based on the Richardson extrapolation method was used to evaluate the truncation error and computational accuracy caused by the computational grid [30]. When using the GCI for judgment, the number of grid groups should be greater than or equal to three [31,32]. In this paper, three grid schemes were simulated. The number of grids was 563,013, 843,844, and 1,628,496, respectively. The encryption factors  $r_{21}$  and  $r_{32}$  of grid scheme 1 were about 1.25 and 1.33, respectively, when compared with those of grid scheme 2 and grid scheme 3. The extrapolated relative errors of section velocity  $v$  were 1.013% and 0.639%, respectively, and the GCI was also less than 5%. It can be seen from Table 1 that with the mesh encryption, the GCI values gradually decreased, and all of them were less than 5%, indicating that the grid in this scheme had smaller discrete errors and that it could be used as a grid for the numerical calculation.

Table 1. GCI calculation result.

Total Number of Grid Points	$r(D_K/D_{K+1})$	$v$	$e_a/\%$	$GCI = \frac{1.25e_a}{r^p - 1}$
563,013		0.790		
843,844	1.250	0.782	1.013	1.131
1,628,496	1.333	0.777	0.639	0.497

#### 2.4. Numerical Simulation Reliability Verification

In order to analyze the reliability of the numerical simulation, it was carried out under the original scheme, and the numerical simulation results were compared with the model

test results. According to the flow pattern analysis of the characteristic section of the box culvert by numerical simulation, it could be seen that the water flow would reflux at the bottom of the box culvert and below the deflecting flow baseplate and that the water flow would shunt at the front end of the long diversion pier. The results are in agreement with the model test results, indicating that the established numerical model can accurately simulate the flow pattern of the eccentric tapering outlet pressure box culvert.

In order to further quantitatively analyze the reliability of the numerical simulation, the same section was selected from the numerical model as that from the model test, and the accuracy of the numerical model was analyzed by comparing the axial velocity of the measuring points. In this paper, the axial velocity of the measuring point was taken as the control index, and the measuring vertical lines 1–6 were evenly arranged at the water outlets of the two pressure ducts. Each measuring line was arranged with three measuring points, i.e., 0.3 h, 0.6 h, and 0.9 h, respectively, where h was the water depth. The positions of the measuring vertical lines are shown in Figure 7.

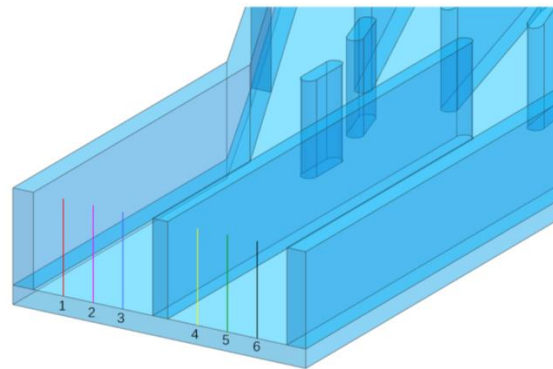


**Figure 7.** Measurement vertical layout: The numbers 1–6 are measuring vertical lines.

The LGY-III multi-functional intelligent flowmeter was used to calculate and convert the flow velocity of the measuring points on the measuring line, and the average flow velocity of each measuring point was obtained. By comparing the velocity data collected by the physical model with those obtained by the numerical simulation, it can be seen from Figure 8 that the experimental data of the physical model and the results of the numerical simulation were in good agreement, which indicates that the numerical simulation conclusions in this paper are credible.

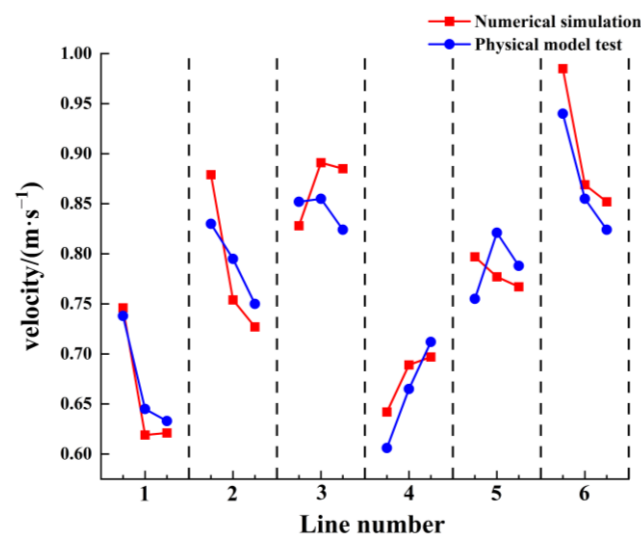


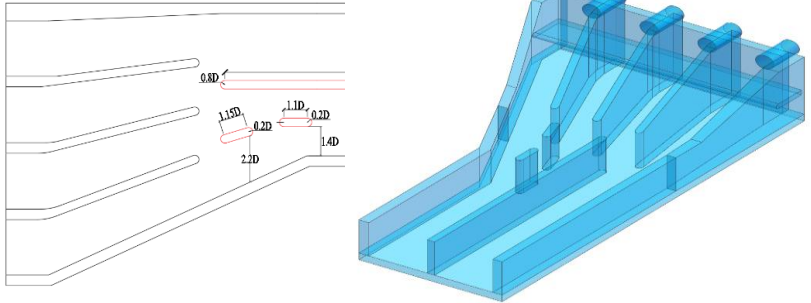
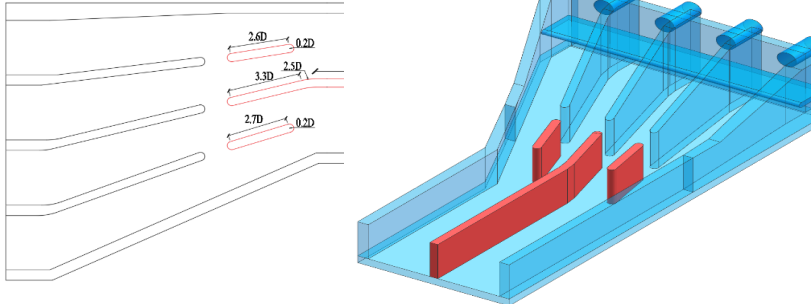
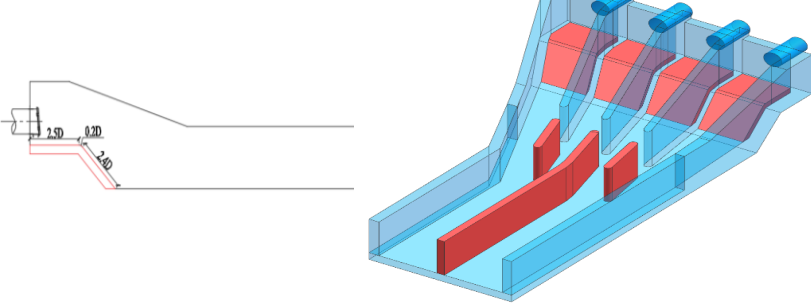
**Figure 8.** Comparison chart of flow velocity at measuring points.

### 3. Analysis and Discussion

#### 3.1. Optimization Scheme Design

The physical model test found that the outlet flow of the unit in the original scheme could not be smooth; this caused a large transverse flow velocity, which in turn led to the formation of poor flow patterns such as bias flow, reflux, and flow separation in the box culvert, forming a large head loss. Due to the limited space in the interior layout of the eccentric tapering outlet pressure box culvert, it was difficult to arrange rectification measures in the interior. Therefore, the proposal was to eliminate the bad flow pattern by optimizing the structural arrangement of the box culvert in order to achieve the purpose of improving the outflow efficiency of the pumping station. Two optimization schemes were proposed, and the structural layout of the optimization scheme is shown in Table 2.

Table 2. Optimization measures in the box culvert.

Scheme	Optimization Measure	Dimension
0	Original scheme	
1	Position and angle of diversion pier	
2	Deflecting flow baseplate	

Optimization scheme 1 proposes a new combined structural arrangement that optimizes the position and water-facing angle of the diversion pier. The inlet end of the long diversion pier is arranged along the flow direction to meet the streamline requirements, and the short diversion piers with lengths of 2.3 D and 2.4 D are arranged on both sides of the long diversion inlet, where D is the diameter of the outlet pipe. On the basis of

optimization scheme 1, optimization scheme 2 optimizes the deflecting flow baseplate under the outlet conduit to make it slope down to the bottom plate of the box culvert.

### 3.2. Characteristic Section Arrangement

In order to further study the hydraulic characteristics inside the box culvert, the characteristic section shown in Figure 9 was selected for analysis.  $Z = 3$  m was selected as the horizontal section A to analyze the hydraulic characteristics of the middle of the box culvert.  $X = 3$  m was selected as the axial section B to analyze the axial hydraulic characteristics of the box culvert. In order to study the transverse bias flow of the outflow of the four units in the shrinking section of the box culvert, four vertical sections, i.e., C, D, E, and F, were selected at  $Y = 19$  m, and quantitative analysis was carried out by calculation. In order to quantitatively compare the optimization effects of each scheme, two vertical sections, G and H, were taken at the outlet of the pressure duct to quantitatively calculate the axial velocity uniformity and the average angle of the axial velocity.

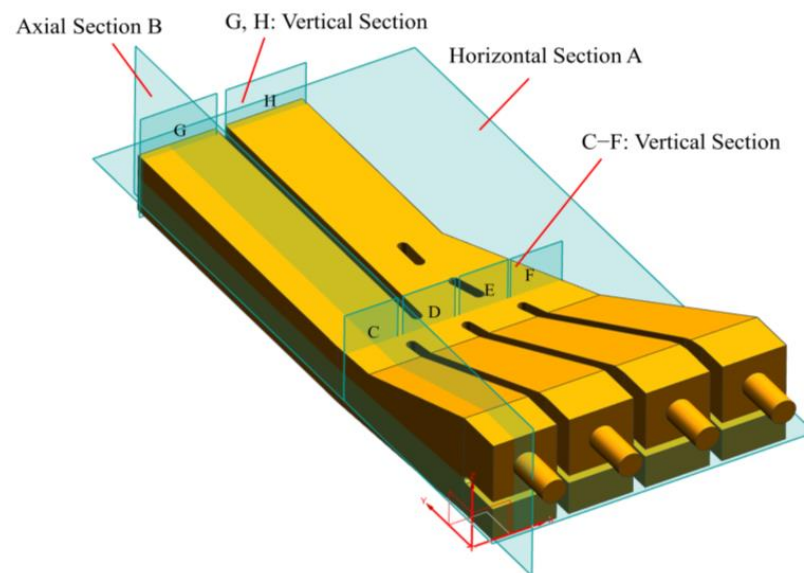


**Figure 9.** Typical section diagram.

### 3.3. Hydraulic Characteristic Analysis

#### 3.3.1. Original Scheme

Figure 10a shows the plane flow field cloud chart of the original scheme outlet box culvert on the horizontal section A. From the flow field diagram, it can be clearly seen that the flow separation will occur at the side wall of the pressure duct and the short diversion pier. This is because the layout of the short diversion pier is unreasonable, and the contraction angle is not consistent with the boundary line required by the flow streamline. Flow separation will occur on the side wall, increasing the transverse flow velocity, resulting in the disorder of the outflow pattern and affecting the outflow efficiency of the pumping station. It can be seen from the streamline diagram that the unit outflow will form a recirculation zone at the front end of the separating pier between unit 3 and unit 4, which will increase the hydraulic loss. The outflow of unit 3 is diverted at the inlet end of the long diversion pier, which cannot completely enter the No.2 pressure duct. Instead, it will be shunted to the right into the No.1 pressure duct, resulting in the imbalance of the flow distribution of the two pressure ducts and forming a pressure difference on both sides of the long diversion pier. When combined with the pressure distribution cloud chart in Figure 10b on the horizontal section A, it was found that there was a large pressure difference on both sides of the inlet end of the long diversion pier and on both sides of the pressure ducts. Figure 10c is the axial flow field cloud diagram of the pressure box culvert under the original scheme. It can be seen from the diagram that the outflow of

the unit cannot completely flow downstream and that a recirculation zone will be formed at the bottom of the box culvert and below the deflecting flow baseplate, resulting in a large head loss. This is because of the unreasonable arrangement of the deflecting flow baseplate structure. The outflow of the unit forms a recirculation zone in the lower layer of the deflecting flow baseplate. At the same time, the outflow of the unit will be blocked by the inclined roof of the box culvert, which will further aggravate the formation of the recirculation zone at the bottom of the box culvert.

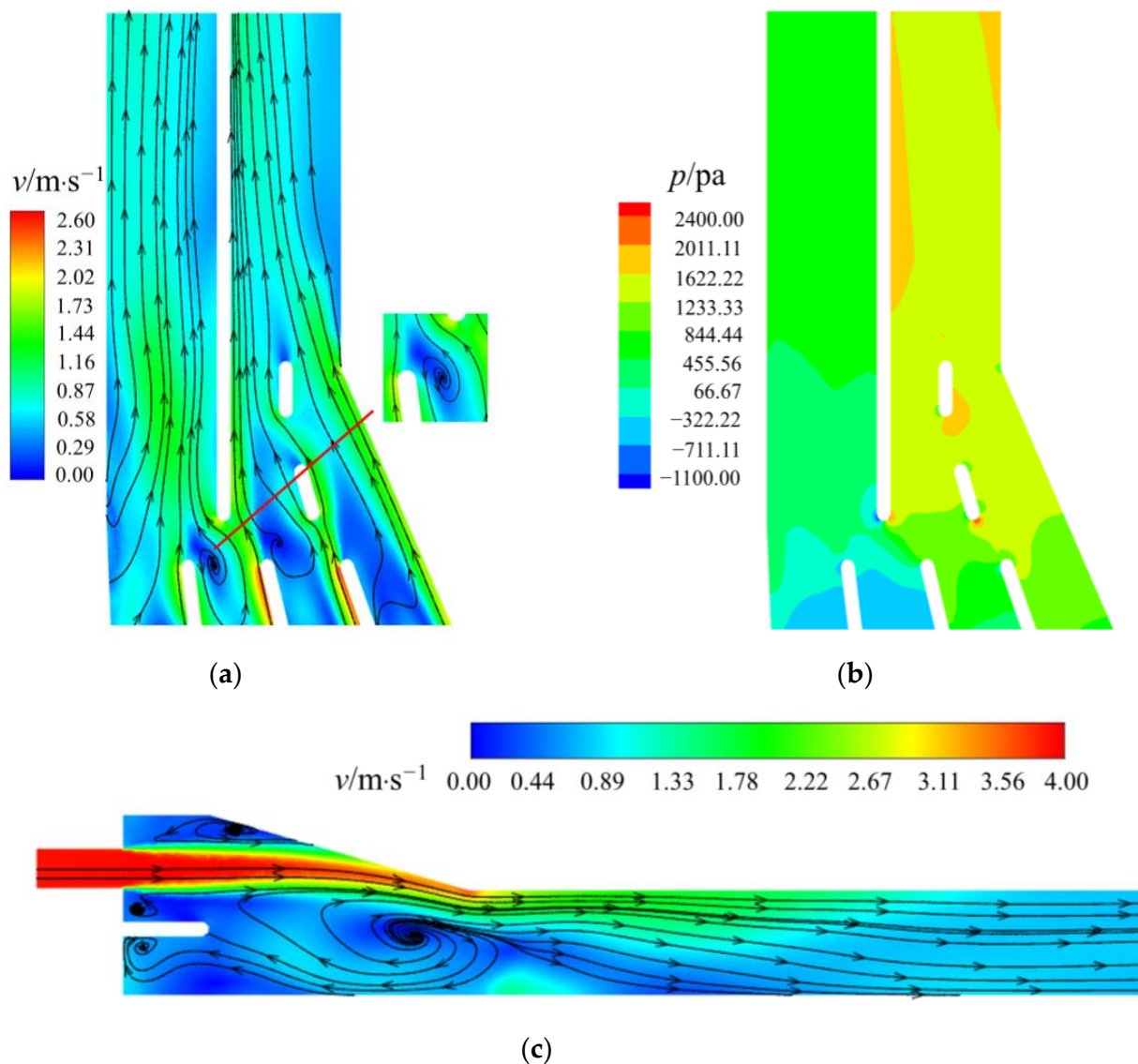


**Figure 10.** Cloud chart of hydraulic characteristics of the original scheme: (a) plane flow field cloud chart; (b) pressure distribution cloud chart; (c) axial flow field cloud chart.

### 3.3.2. Optimization Scheme 1

The cloud diagram of the hydraulic characteristics of optimization scheme 1 is shown in Figure 11. It can be seen from Figure 11a that after optimizing the location and angle of the diversion pier, the flow separation phenomenon on the side wall of the pressure ducts and near the short diversion pier is improved. The recirculation zone at the front end of the separating pier between unit 3 and unit 4 disappears. The outflow of unit 3 does not diverge at the entrance of the long diversion pier and can flow into the No.2 pressure duct along the diversion pier, which improves the uneven excess flow on both sides of the pressure duct. When combined with the pressure distribution cloud chart of Figure 11b, it

can be clearly seen that the pressure on both sides of the long diversion pier is basically equal, but the pressure distribution in the No.1 pressure duct is uneven. According to the Figure 11c axial flow field cloud diagram, it was found that, compared with the original scheme, there was still a backflow area under the deflecting flow baseplate and that the outflow would form a wider range of backflow area in the bottom plate of the box culvert, which would bring greater head loss.

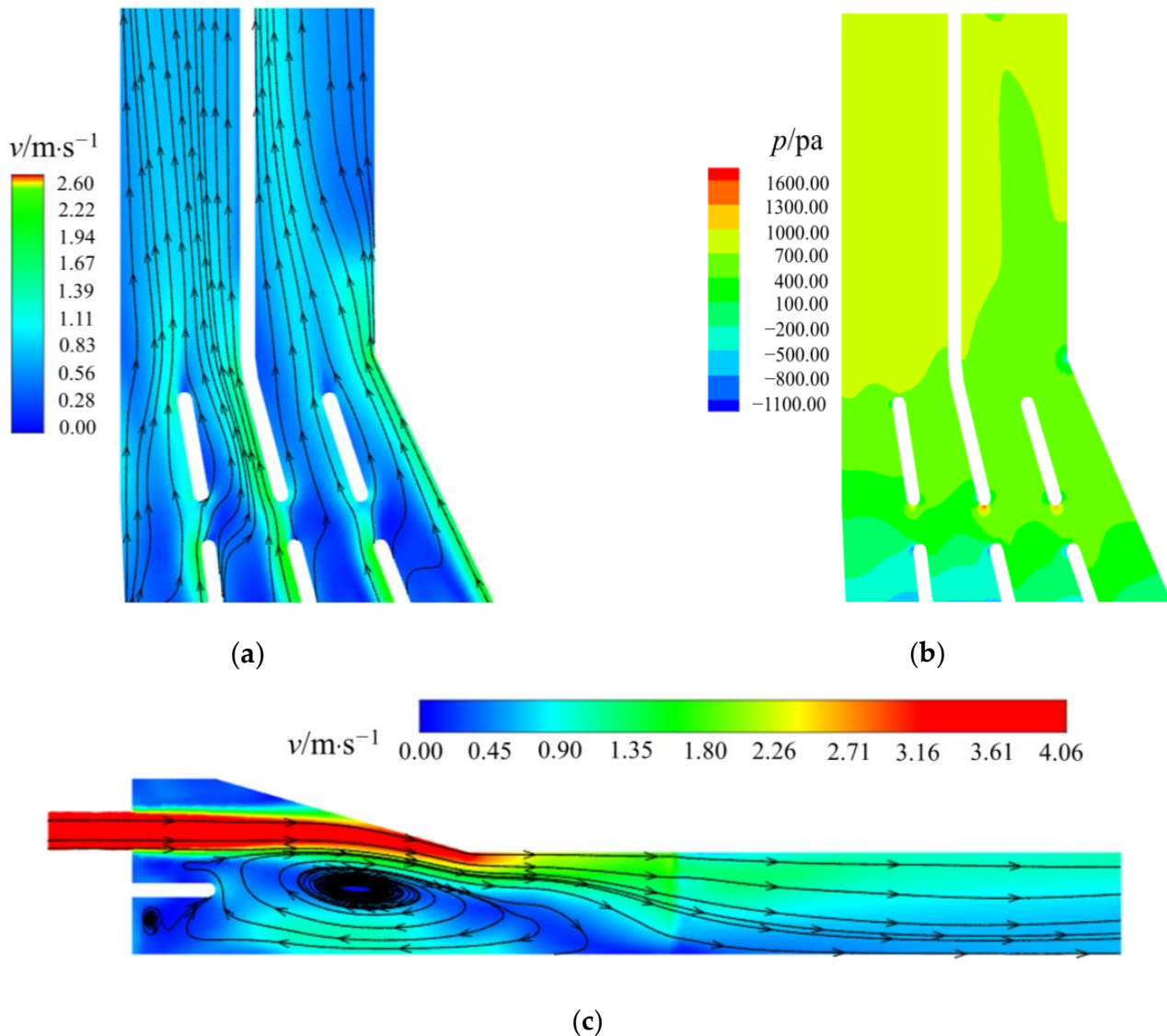


**Figure 11.** Cloud chart of hydraulic characteristics of optimization scheme 1: (a) plane flow field cloud chart; (b) pressure distribution cloud chart; (c) axial flow field cloud chart.

### 3.3.3. Optimization Scheme 2

On the basis of optimization scheme 1, optimization scheme 2 optimizes the deflecting flow baseplate to make it move obliquely down to the box culvert bottom plate. It can be seen from the axial flow field cloud diagram in Figure 12c that optimization scheme 2 eliminates the recirculation zone under the deflecting flow baseplate in the original scheme, further reduces the recirculation zone at the bottom of the box culvert, and reduces the head loss. As shown in Figure 12a, when compared with the original scheme, the recirculation zone at the front end of the separating pier between unit 3 and unit 4 disappears. From the streamline diagram, it can be clearly seen that there is no flow separation at the side wall of the pressure ducts and near the short diversion pier and that no large transverse bias will be

generated, thus improving the discharge efficiency of the pumping station. The outflow of unit 3 does not have an obvious diversion at the inlet end of the long diversion pier, which improves the phenomenon of uneven overflow in the two pressure ducts. When combined with Figure 12b, it can be seen that the pressure is relatively uniformly distributed in the two pressure ducts compared to that of the rest of the schemes.

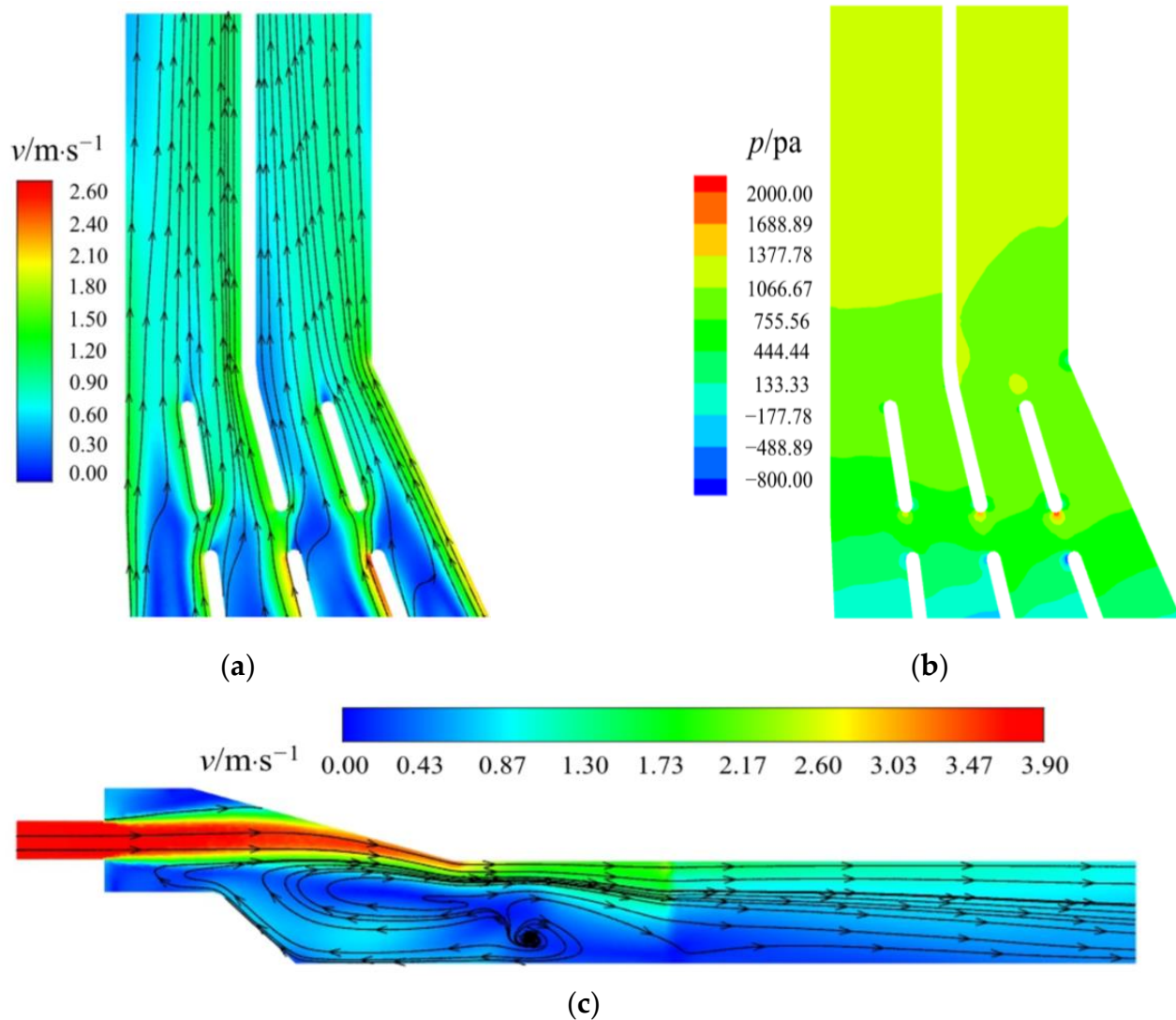


**Figure 12.** Cloud chart of hydraulic characteristics of optimization scheme 2: (a) plane flow field cloud chart; (b) pressure distribution cloud chart; (c) axial flow field cloud chart.

### 3.4. Quantitative Evaluation of Optimization Effect

#### 3.4.1. Transverse Velocity Distribution Ratio

Because of its special structure, in the study of the hydraulic characteristics of the eccentric tapering outlet pressure box culvert, more attention should be paid to the influence of transverse velocity on the flow pattern. In order to quantitatively evaluate the lateral bias flow of the unit outflow under each scheme, four characteristic sections were taken for analysis.

The locations of the characteristic sections are shown in Figure 9. The transverse velocity distribution ratio was used for comparative analysis. The smaller the value is, the

smaller the relative transverse velocity will be and the smaller the transverse bias flow that will be caused. It can be calculated by Equation (5).

$$S = \frac{v_x}{v} \quad (5)$$

where  $v_x$  is transverse velocity, m/s;  $v$  is resultant velocity, m/s.

Figure 13 shows the transverse velocity distribution ratio under each scheme. It can be seen from the figure that both of the optimization schemes can reduce the transverse velocity distribution ratio of the characteristic section. The transverse velocity distribution ratio of the original scheme reached the maximum on the D section, reaching  $-62.50\%$ . When combined with the streamline of Figure 10a, it can be seen that the outflow has an obvious transverse bias flow in this section. Optimization scheme 2 reduces the transverse velocity distribution ratio of the D section to  $-18.82\%$ , which is a reduction of  $43.68\%$ ; thus, the optimization effect is obvious. It can be seen that the optimization scheme has an optimization effect on the transverse bias flow of the characteristic section and that optimization scheme 2 has obvious advantages.

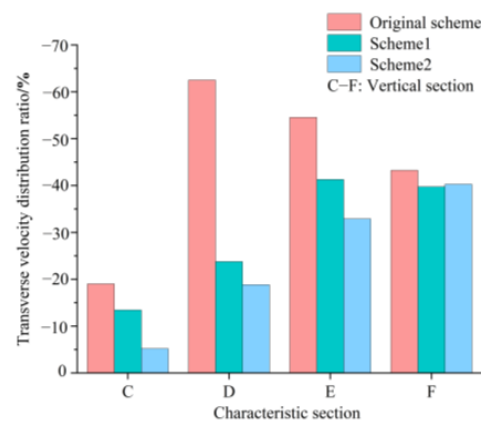


**Figure 13.** Transverse velocity distribution ratio of each scheme: The C–F are the vertical sections.

### 3.4.2. Average Angle of the Axial Velocity and Axial Velocity Uniformity

The weighted average angle of axial velocity is used to reflect the angle between the velocity direction and the vertical section. The smoother the axial velocity is, the closer its value is to 90 degrees. The axial velocity uniformity  $v_{au}$  can reflect the uniformity of the velocity distribution on the section. The larger the value, the better the uniformity of velocity on the section. The average angle of the axial velocity and axial velocity uniformity can be calculated by Equations (6) and (7).

$$\theta_a = \frac{\sum_{i=1}^n v_{ai} \left[ 90^\circ - \arctan \frac{v_{ti}}{v_{ai}} \right]}{\sum_{i=1}^n v_{ai}} \quad (6)$$

$$V_{au} = \left[ 1 - \frac{\sqrt{\sum_{i=1}^n (v_{ai}/v_a - 1)^2}}{n} \right] \times 100\% \quad (7)$$

where  $\theta_a$  is the average angle of the axial velocity,  $^\circ$ ;  $v_{au}$  is the axial velocity uniformity;  $v_{ti}$  is the transversal velocity of each mesh node, m/s;  $v_{ai}$  is the axial velocity of each mesh node, m/s; and  $n$  is the number of grid nodes.

As shown in Figure 14,  $v_{xi}$  and  $v_{zi}$  are the velocity of each mesh node in the X and Z directions. The transversal velocity  $v_{ti}$  is the square root of the square sum of  $v_{xi}$ , and  $v_i$  is the velocity of each mesh node.

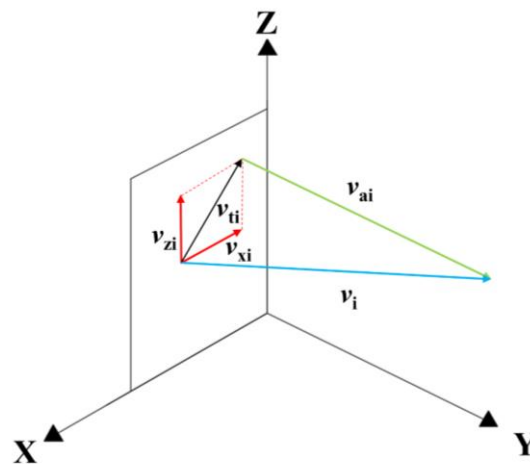


**Figure 14.** Vector diagram of velocity component of grid node.

The characteristic sections G and H of the pressure pipeline outlet were analyzed. The location of the characteristic section is shown in Figure 9. It can be seen from Table 3 that, compared with the original scheme, the optimized scheme can optimize the axial velocity uniformity and average angle of the axial velocity of the characteristic section, making the flow pattern in the pressure duct stable and improving the discharge efficiency of the pumping station. Among the schemes, optimization scheme 2 has the most obvious optimization effect and can increase the uniformity of the axial velocity by 14.97% and the axial weighted average angle of the axial velocity by 7.39°.

**Table 3.** The axial velocity uniformity and average angle of the axial velocity on the characteristic section of each scheme.

Scheme	Section G		Section H	
	$V_{au}/\%$	$\theta_a/^\circ$	$V_{au}/\%$	$\theta_a/^\circ$
Original scheme	69.70	78.38	68.60	80.18
Scheme 1	79.51	84.41	80.04	81.34
Scheme 2	87.15	86.61	81.09	86.73

### 3.4.3. Pressure Distribution

The unreasonable arrangement of the structure in the eccentric tapering outlet pressure box culvert will lead to the problem of different distribution flows on both sides of the pressure duct, resulting in the pressure difference on both sides of the long diversion pier. Therefore, it is necessary to quantitatively analyze the pressure on both sides of the long diversion pier. This paper evaluates the optimization effect of each scheme by comparing the pressures of the specific measuring points. The measurement points are located on both sides of the long diversion pier and arranged on the horizontal section A. The distances in the Y direction are  $Y = 21$  m,  $Y = 26$  m,  $Y = 31$  m,  $Y = 36$  m, and  $Y = 41$  m. In Figure 15, the left and right sides are used to indicate the position of the measuring point on the long diversion pier.

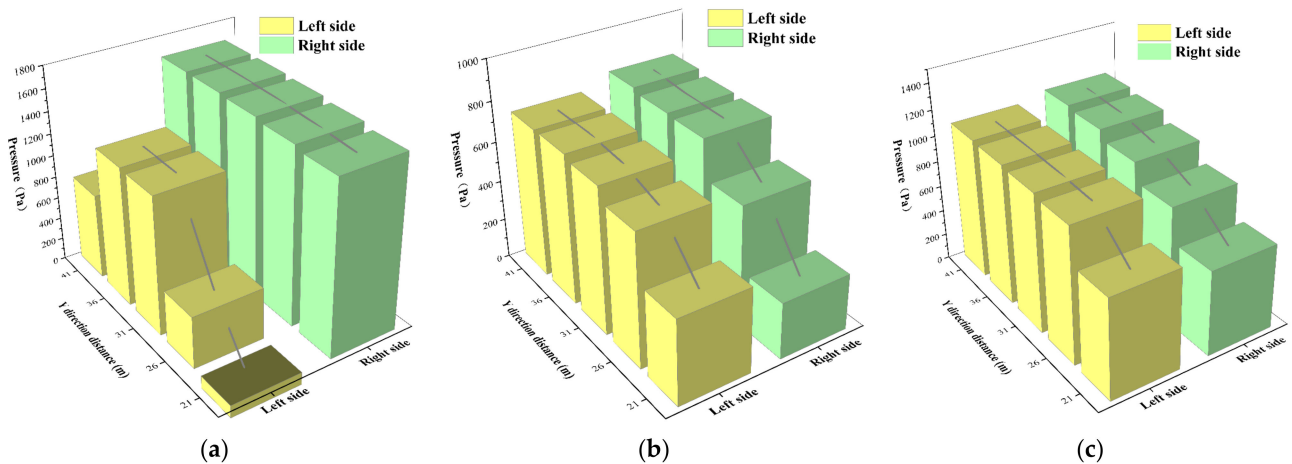


**Figure 15.** Pressure distribution on both sides of long diversion pier: (a) original scheme; (b) scheme 1; (c) scheme 2.

As can be seen from Figure 15, in the original scheme, there was a pressure difference on both sides of the long diversion pier, and the pressure difference reached its maximum at  $Y = 21$  m, which is 1679.51 Pa. However, the pressure on the left side of the long diversion pier was much less than that on the right side, resulting in a pressure difference on both sides of the long diversion pier. Optimization scheme 2 can minimize the pressure difference on both sides of the long diversion pier to 21.21 Pa and make the pressure distribution on both sides more uniform. It can be seen that the optimization scheme has an optimization effect on the uneven pressure distribution on both sides of the long diversion pier and that optimization scheme 2 has the best optimization effect.

### 3.5. The Best Scheme

Through the above research, it was determined that optimization scheme 2 was the best scheme. In order to further verify the optimization effect of scheme 2, the axial velocity of the measuring point at the exit section was compared with the theoretical average velocity. The theoretical average velocity can be calculated by Equation (8).

$$v_t = \frac{Q}{S} \quad (8)$$

where  $Q$  is the flow rate,  $\text{m}^3/\text{s}$ ;  $S$  is the characteristic section area,  $\text{m}^2$ .

The results are shown in Figure 16.  $X$  is the dimensionless number of the relative position of the outlet section,  $X = \frac{x}{D}$ ;  $D$  is the diameter of the outlet pipe, m; and  $x$  is the horizontal distance from the coordinate origin to the measuring point, m.

It can be seen from Figure 16 that the velocity distribution of each measurement point under optimization scheme 2 is more uniform and that the velocity of each measurement point is closer to the theoretical average velocity, which is obviously better than the original scheme, indicating that the velocity uniformity of the measurement point under optimization scheme 2 is better.

In order to quantitatively describe the velocity distribution uniformity of the measuring points, the mean square error of each scheme is calculated, which can be calculated by Equation (9).

$$MSE = \frac{1}{n} \sum_{i=1}^n (v - v_t)^2 \quad (9)$$

where  $MSE$  is mean square error;  $n$  is the number of measuring points;  $v$  is the velocity of measuring points,  $\text{m}^3/\text{s}$ ;  $v_t$  is the theoretical average velocity,  $\text{m}^3/\text{s}$ .

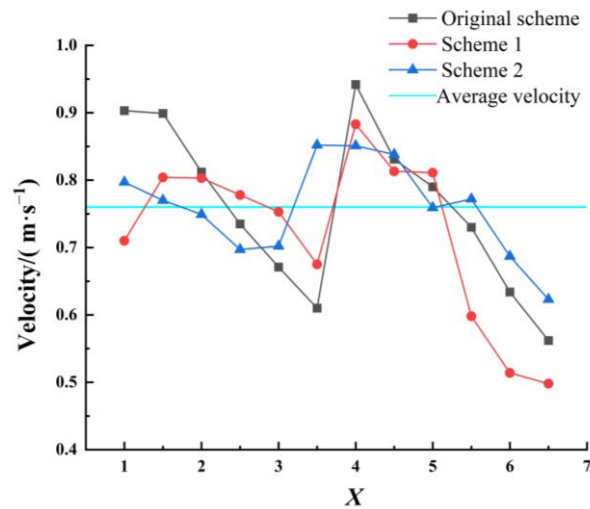


Figure 16. Measurement point velocity distribution diagram.

The mean square error of scheme 2 is 0.00467, and the mean square error of the original scheme is 0.014. It can be considered that the uniformity of the measuring points of scheme 2 is better.

#### 4. Conclusions

The optimization of the box culvert flow pattern can reduce head loss and improve the discharge efficiency of a pumping station. In this paper, a variety of optimization schemes were proposed, including schemes that optimized the position and angle of the diversion pier and optimized the structure of the deflecting flow baseplate. After the accuracy of the numerical simulation was verified by the model test, the flow pattern, transverse velocity distribution ratio, pressure distribution, average angle of the axial velocity, and axial velocity uniformity of each scheme were obtained by numerical simulation calculation. When combined with each evaluation index, the optimization effect of each optimization scheme on the flow pattern was compared, and the following conclusions could be drawn:

- (1) In the absence of optimization measures, there are adverse flow patterns, such as bias flow, reflux, and flow separation, inside the eccentric tapering outlet pressure box culvert, which will increase the head loss and affect the outlet efficiency of the pumping station;
- (2) All the optimization schemes can improve the flow pattern of the eccentric tapering outlet pressure box culvert. Among them, the combination scheme of “diversion pier position and angle with deflecting flow baseplate” has the best optimization effect, as it significantly improves the bad flow pattern and makes the outlet velocity distribution uniform. The transverse velocity distribution ratio was reduced, especially on the characteristic section D, which was reduced by 43.68%. The axial velocity uniformity and the average angle of the axial velocity were increased by 14.97% and 7.39° on average. The pressure distribution was more uniform, and the minimum pressure difference on both sides of the long diversion pier was reduced to 21.21 Pa;
- (3) It is of great significance to synthesize evaluation indexes for the optimization of hydraulic structure. The evaluation indexes proposed in this paper has guiding significance for the analysis of hydraulic characteristics in hydraulic engineering and the comparison and selection of optimal schemes. In particular, it provides optimization schemes and new evaluation indexes for the optimization of eccentric tapering outlet pressure box culvert in the expanded pumping station. In view of the advantages of the new optimization scheme and evaluation index, it is worth further promotion and consideration;

- (4) Our research illustrates that the combination scheme of “diversion pier position and angle with deflecting flow baseplate” is an effective scheme to improve the bad flow pattern when the four units are running at the same time. However, it should be noted that the current research is only based on limited conditions. In the future, in-depth researches can be carried out for different unit operating conditions to ensure that there will still be no bad flow patterns in the box culvert under wider range of conditions. Therefore, the future research focus should be placed on the size and length of diversion pier and deflecting flow baseplate under multiple working conditions.

**Author Contributions:** Conceptualization, B.X.; methodology, B.X. and Z.C.; software, Y.-X.C. and Z.C.; original draft preparation, Y.-X.C.; writing—review and editing, B.X. and Y.-X.C.; experiments, Y.-X.C., Z.C. and S.S.; investigation, B.X. All authors have read and agreed to the published version of the manuscript.

**Funding:** This research was funded by the National Natural Science Foundation of China (grant No. 51541912), Postgraduate Research & Practice Innovation Program of Jiangsu Province (grant no. SJCX22\_1760), and National science and technology support program project of China (grant No. 2102BOD08B03-2).

**Data Availability Statement:** Not applicable.

**Conflicts of Interest:** The authors declare no conflict of interest.

## References

- Kan, K.; Zhang, Q.; Xu, Z.; Chen, H.; Zheng, Y.; Zhou, D.; Binama, M. Study on a horizontal axial flow pump during runaway process with bidirectional operating conditions. *Sci. Rep.* **2021**, *11*, 1–21. [[CrossRef](#)]
- Luo, C.; Du, K.; Qi, W.; Cheng, L.; Huang, X.; Lu, J. Investigation on the effect of the shaft transition form on the inflow pattern and hydrodynamic characteristics of the pre-shaft tubular pump device. *Front. Energy Res.* **2022**, *10*, 955492. [[CrossRef](#)]
- Shi, L.; Zhang, W.; Jiao, H.; Tang, F.; Wang, L.; Sun, D.; Shi, W. Numerical simulation and experimental study on the comparison of the hydraulic characteristics of an axial-flow pump and a full tubular pump. *Renew. Energy* **2020**, *153*, 1455–1464. [[CrossRef](#)]
- Shi, L.; Zhu, J.; Tang, F.; Wang, C. Multi-disciplinary optimization design of axial flow pump impellers based on the approximation model. *Energies* **2020**, *13*, 779. [[CrossRef](#)]
- Yang, F.; Li, Z.; Yuan, Y.; Lin, Z.; Zhou, G.; Ji, Q. Study on vortex flow and pressure fluctuation in dustpan-shaped conduit of a low head axial-flow pump as turbine. *Renew. Energy* **2022**, *196*, 856–869. [[CrossRef](#)]
- Zhou, J.; Zhao, M.; Wang, C.; Gao, Z. Optimal Design of Diversion Piers of Lateral Intake Pumping Station Based on Orthogonal Test. *Shock Vib.* **2021**, *2021*, 6616456. [[CrossRef](#)]
- Zhou, J.; Zhong, Z.; Liang, J.; Shi, X. Three-dimensional Numerical Simulation of Side-intake Forebay of Pumping Station. *J. Irrig. Drain.* **2015**, *34*, 52–55.
- Zi, D.; Wang, F.; Yao, Z.; Hou, Y.; Yang, E. Effects analysis on rectifying intake flow field for large scale pumping station with combined diversion piers. *Trans. Chin. Soc. Agric. Eng.* **2015**, *31*, 71–77.
- Song, W.; Pang, Y.; Shi, X.; Xu, Q. Study on the Rectification of Forebay in Pumping Station. *Math. Probl. Eng.* **2018**, *2018*, 2876980. [[CrossRef](#)]
- Can, L.; Chao, L. Numerical simulation and improvement of side-intake characteristics of multi-unit pumping station. *J. Hydroelectr. Eng.* **2015**, *34*, 207–214.
- Luo, C.; Qian, J.; Liu, C.; Chen, F.; Xu, J.; Zhou, Q. Numerical simulation and test verification on diversion pier rectifying flow in forebay of pumping station for asymmetric combined sluice-pump station project. *Trans. Chin. Soc. Agric. Eng.* **2015**, *31*, 100–108.
- Kadam, P.; Chavan, D. CFD Analysis of Flow in Pump Sump to Check Suitability for Better Performance of Pump. *Int. J. Mech. Eng. Robot.* **2013**, *1*, 59–65.
- Zhao, H.; Yang, F.; Liu, C.; Chen, S.; He, J. Numerical simulation of side-intake flow for fluid meliorating of pumping stations. *Water Resour. Hydropower Eng.* **2017**, *48*, 79–84.
- Zhang, Y.; Song, S.; Chen, Y.; Liu, X.; Fu, X. Numerical Simulation of Rectification Measures for Side-direction Forebay in Pump Station. *China Rural Water Hydropower* **2016**, *5*, 117–120.
- Chen, H.-X.; Guo, J.-H. Numerical simulation of 3-D turbulent flow in the multi-intakes sump of the pump station. *J. Hydrodyn.* **2007**, *19*, 42–47. [[CrossRef](#)]
- Xia, C.; Cheng, L.; Zhao, G.; Yu, L.; Wu, M.; Xu, W. Numerical simulation of flow pattern in forebay of pump station with single row of square columns. *Adv. Sci. Technol. Water Resour.* **2017**, *37*, 53–58.
- Nguyen, V.; Vo, T. Centrifugal Pump Design: An Optimization. *Eurasia Proc. Sci. Technol. Eng. Math.* **2022**, *17*, 136–151. [[CrossRef](#)]
- Chen, Z.; Nguyen, V.; Inagaki, M.; Choi, Y.D. Performance of an Open Ducted Type Very Low Head Cross-Flow Turbine. *GMSARN Int. J.* **2015**, *9*, 23–28.

19. Yang, F.; Zhang, Y.; Liu, C.; Wang, T.; Jiang, D.; Jin, Y. Numerical and Experimental Investigations of Flow Pattern and Anti-Vortex Measures of Forebay in a Multi-Unit Pumping Station. *Water* **2021**, *13*, 935. [[CrossRef](#)]
20. Luo, C.; He, Y.; Shang, Y.; Cong, X.; Ding, C.; Cheng, L.; Lei, S. Flow Characteristics and Anti-Vortex in a Pump Station with Laterally Asymmetric Inflow. *Processes* **2022**, *10*, 2398. [[CrossRef](#)]
21. Xu, W.; Cheng, L.; Du, K.; Yu, L.; Ge, Y.; Zhang, J. Numerical and Experimental Research on Rectification Measures for a Contraction Diversion Pier in a Pumping Station. *J. Mar. Sci. Eng.* **2022**, *10*, 1437. [[CrossRef](#)]
22. Nasr, A.; Yang, F.; Zhang, Y.; Wang, T.; Hassan, M. Analysis of the Flow Pattern and Flow Rectification Measures of the Side-Intake Forebay in a Multi-Unit Pumping Station. *Water* **2021**, *13*, 2025. [[CrossRef](#)]
23. Zhang, C.; Yan, H.; Jamil, M.T.; Yu, Y. Improvement of the Flow Pattern of a Forebay with a Side-Intake Pumping Station by Diversion Piers Based on Orthogonal Test Method. *Water* **2022**, *14*, 2663. [[CrossRef](#)]
24. Ansar, M.; Nakato, T. Experimental study of 3D pump-intake flows with and without cross flow. *J. Hydrol. Eng.* **2001**, *127*, 825–834. [[CrossRef](#)]
25. Rajendran, V.; Constantinescu, S.; Patel, V. Experimental validation of numerical model of flow in pump-intake bays. *J. Hydraul. Eng.* **1999**, *125*, 1119–1125. [[CrossRef](#)]
26. Caishui, H. Three-dimensional Numerical Analysis of Flow Pattern in Pressure Forebay of Hydropower Station. *Procedia Eng.* **2012**, *28*, 128–135. [[CrossRef](#)]
27. Xiao, H.; Wang, J.; Liu, Z.; Liu, W. A consistent SIMPLE algorithm with extra explicit prediction—SIMPLEPC. *Int. J. Heat Mass Transf.* **2018**, *120*, 1255–1265. [[CrossRef](#)]
28. Shaheed, R.; Mohammadian, A.; Gildeh, H.K. A comparison of standard  $k-\epsilon$  and realizable  $k-\epsilon$  turbulence models in curved and confluent channels. *Environ. Fluid Mech.* **2019**, *19*, 543–568. [[CrossRef](#)]
29. Xu, B.; Liu, J.; Lu, W. Optimization Design of Y-Shaped Settling Diversion Wall Based on Orthogonal Test. *Machines* **2022**, *10*, 91. [[CrossRef](#)]
30. Stern, F.; Wilson, R.V.; Coleman, H.W.; Paterson, E.G. Comprehensive Approach to Verification and Validation of CFD Simulations—Part 1: Methodology and Procedures. *J. Fluid Mech.* **2001**, *123*, 792. [[CrossRef](#)]
31. Savage, B.M.; Crookston, B.M.; Paxson, G.S. Physical and Numerical Modeling of Large Headwater Ratios for a 15 Labyrinth Spillway. *J. Hydraul. Eng.* **2016**, *142*, 04016046. [[CrossRef](#)]
32. Liu, H.; Liu, M.; Bai, Y.; Du, H.; Dong, L. Grid convergence based on GCI for centrifugal pump. *J. Jiangsu Univ.* **2014**, *35*, 279–283.

**Disclaimer/Publisher’s Note:** The statements, opinions and data contained in all publications are solely those of the individual author(s) and contributor(s) and not of MDPI and/or the editor(s). MDPI and/or the editor(s) disclaim responsibility for any injury to people or property resulting from any ideas, methods, instructions or products referred to in the content.